
Article:
Eatson, J.W. orcid.org/0000-0002-5160-8871, Parker, R.J. orcid.org/0000-0002-1474-7848 and Lichtenberg, T. orcid.org/0000-0002-3286-7683 (2024) Toward a unified injection model of short-lived radioisotopes in N-body simulations of star-forming regions. The Astrophysical Journal, 977 (1). 13. ISSN 0004-637X

https://doi.org/10.3847/1538-4357/ad8642

The Astrophysical Journal, 977:13 (11pp), 2024 December 10 https://doi.org/10.3847/1538-4357/ad8642

Toward a Unified Injection Model of Short-lived Radioisotopes in *N*-body Simulations of Star-forming Regions

Joseph W. Eatson[1], Richard J. Parker[1,3], and Tim Lichtenberg[2]
[1] Department of Physics and Astronomy, The University of Sheffield, Hicks Building, Hounsfield Road Sheffield, S3 7RH, UK
[2] Kapteyn Astronomical Institute, University of Groningen, P.O. Box 800, 9700 AV Groningen, The Netherlands
Received 2024 June 24; revised 2024 October 8; accepted 2024 October 10; published 2024 November 28

Abstract

Recent research provides compelling evidence that the decay of short-lived radioisotopes (SLRs), such as ^{26}Al, provided the bulk of energy for heating and desiccation of volatile-rich planetesimals in the early solar system. However, it remains unclear whether the early solar system was highly enriched relative to other planetary systems with similar formation characteristics. While the solar system possesses an elevated level of SLR enrichment compared to the interstellar medium, determining SLR enrichment of individual protoplanetary disks observationally has not been performed and is markedly more difficult. We use *N*-body simulations to estimate enrichment of SLRs in star-forming regions through two likely important SLR sources: stellar winds from massive stars and supernovae (SNae). We vary the number of stars and the radii of the star-forming regions and implement two models of stellar-wind SLR propagation for the radioisotopes ^{26}Al and ^{60}Fe. We find that for ^{26}Al enrichment the solar system is at the upper end of the expected distribution, while for the more SNae-dependent isotope ^{60}Fe we find that the solar system is comparatively very highly enriched. Furthermore, combined with our previous research, these results suggest that the statistical role of ^{26}Al-driven desiccation on exoplanet bulk composition may be underestimated in typical interpretations of the low-mass exoplanet census, and that ^{60}Fe is even less influential as a source of heating than previously assumed.

Unified Astronomy Thesaurus concepts: N-body simulations (1083); Planetesimals (1259); Star forming regions (1565); Protoplanetary disks (1300); Planet formation (1241)

1. Introduction

^{26}Al and ^{60}Fe, as well as other short-lived radioisotopes (SLRs), have a significant impact on the formation and evolution of planets, in particular through their influence on planetesimal and protoplanet evolution (T. Lichtenberg et al. 2019, 2023). As these isotopes have a half-life commensurate with planetary formation timescales (0.717 Myr for ^{26}Al, and 2.6 Myr for ^{60}Fe, which compares to observations of (proto) planets around 1 Myr old stars; F. O. Alves et al. 2020; D. M. Segura-Cox et al. 2020), they are present throughout the early planetesimal-formation process, concentrating on planetesimals and debris as the disk agglomerates into a protoplanetary system (S. Krijt et al. 2023). SLRs are important for planetary formation as they provide a significant source of heating through radioactive decay for nascent protoplanets and planetesimals. This can increase the rate of chemical segregation within a forming protoplanet (K. H. Dodds et al. 2021), and is instrumental in the evaporation and removal of volatiles from planetesimals through outgassing (J. Monteux et al. 2018; M. E. Newcombe et al. 2023; D. S. Grewal et al. 2024). Volatile outgassing is of particular interest, as removal of H_2O and other atmospheric volatiles from planetesimals prior to protoplanetary formation can significantly impact the formation of extrasolar ocean worlds, and instead lead to relatively volatile-poor rocky worlds (T. Lichtenberg & S. Krijt 2021; T. Lichtenberg & M. S. Clement 2022).

It has been found that the solar system has a significantly higher fraction of both ^{26}Al and ^{60}Fe than the interstellar medium (ISM; N. T. Kita et al. 2013), with an isotopic ratio $^{26}\mathrm{Al}/^{27}\mathrm{Al}$ ($Z_{26\mathrm{Al}}$) of $\approx 5 \times 10^{-5}$ based on observations of decay products in chondritic meteorites (B. Jacobsen et al. 2008; N. T. Kita et al. 2013). The measurement of ^{60}Fe is much more controversial, though recent estimates (e.g., D. L. Cook et al. 2021) suggest an isotopic ratio $^{60}\mathrm{Fe}/^{56}\mathrm{Fe}$ ($Z_{60\mathrm{Fe}}$) of $\approx 1 \times 10^{-6}$, which is also significantly higher than estimates of the abundance of this isotope in the ISM.

Some researchers have suggested that the parent giant molecular cloud of the solar system had a higher level of SLR enrichment compared to the ISM, due to sequential star formation (M. Gounelle & G. Meynet 2012), whereas other authors have proposed either internal production or delivery from an external source. Although ^{26}Al can be produced internally through cosmic-ray spallation, this is insufficient and does not reflect the isotropic spatial distribution we observe in the SLR distribution in the solar system nor the fractionation between spallation and nucleosynthetic processes (M. Lugaro et al. 2018; R. J. Parker 2020). ^{60}Fe cannot be produced via cosmic-ray spallation (M. Lugaro et al. 2018).

Instead, one of the main proposed external delivery methods is through stellar winds, in which significant quantities of ^{26}Al are produced in the cores of massive stars (A. Palacios et al. 2005; E. Gaidos et al. 2009), the convective core circulates ^{26}Al to the surrounding envelope, and is expelled as a part of the stellar wind. While some ^{60}Fe can be emitted through massive stellar winds, this quantity is many orders of magnitude lower than the total wind mass of ^{26}Al (M. Limongi & A. Chieffi 2018; H. E. Brinkman et al. 2021). Additionally,

[3] Royal Society Dorothy Hodgkin fellow.

large quantities of ^{26}Al and ^{60}Fe are also deposited through supernovae (SNae); however, massive stars take upwards of 10 Myr to explode (M. Limongi & A. Chieffi 2018), by which time disks are likely already far into producing protoplanets, preventing efficient isotope transfer from the outflow to the planetary system before planetesimal formation (J. Drazkowska et al. 2023; C. F. Manara et al. 2023). Finally, there is additional evidence to suggest that a third category of enrichment is potentially important, which is the case of the winds of "interloping" asymptotic giant branch (AGB) stars depositing SLRs into a recently formed star-forming region (A. I. Karakas & M. Lugaro 2016; G. J. Wasserburg et al. 2017). AGB stars wandering into star-forming regions have been observed (R. J. Parker & C. Schoettler 2023), however there has been limited study on the impact of such interlopers, or the probability of this occurring with a star-forming region.

In this paper, we report the results of a series of *N*-body simulations of star-forming regions using `AMUSE` (F. I. Pelupessy et al. 2013) where massive stellar winds and SNae inject ^{26}Al and ^{60}Fe into protoplanetary disks surrounding low-mass stars. The region size, population, and density are varied significantly for each subset of simulations to explore the star-forming region parameter space. This model utilizes wind and SN mass-loss rates of SLRs from work by M. Limongi & A. Chieffi (2018), as well as statistical models of star-forming regions and stellar populations. Our model aims to be more comprehensive than previous attempts to simulate SLR injection within star-forming regions (R. B. Nicholson & R. J. Parker 2017; S. P. Zwart 2019; R. J. Parker et al. 2023) by including all facets of massive star-based SLR injection, though there are a number of additional features and avenues of research that we will discuss in brief at the end of the paper. The following section details the methodology of our work, in particular the programming framework and implementation of various simulation features. Section 3 details our results, Section 4 discusses these results, and Section 5 discusses further research into this particular topic.

2. Methodology

The simulation code used throughout this paper is written in Python, using the `AMUSE` framework to incorporate pre-existing stellar evolution and *N*-body dynamics code. At the beginning of every time step, the code calculates positions and velocities for each star in the simulated region, as well as the individual star properties such as mass-loss rates. The stellar properties are calculated using the `SeBa` stellar-evolution code (S. F. Portegies Zwart & F. Verbunt 1996; S. Toonen et al. 2012), while the dynamical properties are calculated using the `BHTree` *N*-body code (J. Barnes & P. Hut 1986). These properties are then utilized by the Python sections of the code authored for this paper, which calculate enrichment through massive stellar winds and SNae. In addition to this section, code to determine initial mass functions (IMFs) and disk lifetimes was devised, and will be discussed in brief as well.

2.1. General Operation and `AMUSE`

The `AMUSE` framework was used in the simulations in this paper to initialize, translate, and manage the external *N*-body and stellar-evolution codes (S. Portegies Zwart et al. 2009; F. I. Pelupessy et al. 2013; S. F. Portegies Zwart et al. 2013; S. P. Zwart & S. McMillan 2018). While the *N*-body and stellar-evolution codes in `AMUSE` can be bridged and run alongside each other, the code written to calculate SLR enrichment cannot be run synchronously. As such, the main execution loop is divided into a series of time steps so that the enrichment routines can run in lockstep with the rest of `AMUSE`. As closer encounters between stars are fleeting when compared to the simulation timescale, a relatively small time step is adopted in order to sample wind injection more accurately. We found that a total number of 1000 time steps for the enrichment code over 20 Myr was suitable for our simulations, while the *N*-body and stellar-evolution codes operate on smaller time steps.

The `SeBa` stellar-evolution code was utilized to calculate mass-loss rates for main- and post-main-sequence evolution of stars within a star-forming region. `SeBa` is extremely fast, using an interpolated look-up table for stellar evolution rather than directly calculating the stars's properties—such as in the case of a Henyey code like `MESA` (S. F. Portegies Zwart & F. Verbunt 1996; B. Paxton et al. 2011; S. Toonen et al. 2012). While this approximation method is less accurate, `SeBa` is suitable for this work due to its speed. It is important to note that mass-loss rates due to winds can vary significantly between stellar-evolution models. However, a common factor between all models is that the bulk of mass loss over the lifespan of a particularly massive star occurs after the main sequence, which is itself a comparatively short period of time (0.5–1 Myr); as such most enrichment will occur over this time, and should not vary significantly between models. `SeBa` is also used to determine whether massive stars have undergone SNae. Dynamic evolution of the star-forming region is performed using the `BHTree` *N*-body code. `BHTree` is a second-order-accurate Barnes–Hut octree code designed for large numbers of particles. While pure *N*-body codes are more accurate, the extremely favorable scaling characteristics ($\mathcal{O}(N \log N)$ versus $\mathcal{O}(N^2)$ of pure solvers) allow hundreds of large-scale simulations to be run within an acceptable length of time on a 10-core Xeon workstation (J. Barnes & P. Hut 1986). As such, the reduction in accuracy was deemed an acceptable trade-off for this project. Performance was further improved by using `OpenMPI` to multithread `BHTree` (E. Gabriel et al. 2004). At every time step the change in mass calculated through `SeBa` was synchronized with `BHTree` to account for mass loss affecting gravitational attraction.

After the *N*-body solver and stellar-evolution simulations are evolved to the next time step, the code written for this paper to calculate SLR enrichment is executed, as detailed in Section 2.3.

2.2. Region Formation

Upon program initialization a star-forming region with a given number of stars ($N_\star$) and radius (r_c) is generated via a S. P. Goodwin & A. P. Whitworth (2004) box fractal method. The box fractal model spawns fractals by placing a "root" particle in the center of a cube of side $N_{\rm div}$, which spawns N^3 "leaf" cubes, which can also contain their own "leaf" particles. The probability of each generation producing offspring is equivalent to $N_{\rm div}^{D-3}$, and fewer generations are produced with a lower fractal dimension parameter, *D*, which is included as an input parameter to the algorithm (S. P. Goodwin & A. P. Whitworth 2004). Lower values of *D* lead to more substructure and a less uniform appearance, while higher values lead to a more homogeneous and spherical appearance. For our simulations

we adopt a fractal dimension of $D = 2.0$, as this gives a moderate amount of substructure, which is observed in many star-forming regions (A. Cartwright & A. P. Whitworth 2004; N. Sánchez & E. J. Alfaro 2009; S. Dib et al. 2018) and in simulations (J. E. Dale et al. 2012, 2013; P. Girichidis et al. 2012). Subsequent dynamical evolution makes it difficult to ascertain the initial degree of substructure in a typical star-forming region (R. J. Parker & M. R. Meyer 2012; E. C. Daffern-Powell & R. J. Parker 2020), but $D = 2.0$ probably lies toward the middle of the distribution of expected values. The initial velocities of the parent particles are drawn from a Gaussian distribution, with a small random component that scales as $N_{\rm div}^{D-3}$ but reduces for each progressive generation. After generating the positions and velocities of the stars within the star-forming region, the masses are calculated from an implementation of the Maschberger IMF (T. Maschberger 2013). The Maschberger IMF is described in the form of a probability density function following the formula

$$P(M_\star) \propto \frac{M_\star}{\mu}^{-\alpha}\left(1 + \left(\frac{M_\star}{\mu}\right)^{1-\alpha}\right)^{-\beta}, \quad (1)$$

where P is the probability, $M_\star$ is the star mass in $M_\odot$, α is the high-mass exponent, β is the low-mass exponent, and μ is the scale parameter. As per Maschberger's prescription, we use values of $\alpha = 2.3$, $\beta = 1.4$, and $\mu = 0.2$. The mass range of the Maschberger prescription is between $0.01\,M_\odot$ and $150\,M_\odot$. When generating a population of stars, we ensure that there is at least one high-mass star ($M_\star \geqslant 13\,M_\odot$) in the resultant region and the IMF routine is repeatedly run until this condition is met (R. B. Nicholson & R. J. Parker 2017). Stochastic sampling of the IMF can result in low-mass stellar populations that (infrequently) contain massive stars (R. J. Parker & S. P. Goodwin 2007). R. B. Nicholson & R. J. Parker (2017) demonstrate that—assuming a standard cluster mass function of the form $N_{\rm clus} \propto M_{\rm clus}^{-2}$—these unusual low-mass populations that contain high-mass stars occur as often as high-mass clusters, which are almost certain to contain massive stars. So while we do not simulate those clusters that do not contain massive stars (because there would be no enrichment), our enrichment distributions should be interpreted for stellar populations where some enrichment can occur.

All stars in the simulation have the same formation time; while there would be some margin of age difference in the stars this would introduce an additional parameter to explore, significantly increasing the required number of simulations. Furthermore, `SeBa` and by extension `AMUSE` cannot be used to simulate mixed-age stellar populations within a single cluster data type. Finally, binarity of massive stars is not modeled, as wind–wind interactions of massive stars and how this affects dust formation and growth are not well established—though in ideal cases there would be a significant increase in ^{26}Al wind abundance (H. E. Brinkman et al. 2023). We will study the effects of massive-star binarity on the enrichment of low-mass stars in a future paper.

2.2.1. Protoplanetary Disks

Each low-mass star (defined as $0.1\,M_\odot \leqslant M_\star \leqslant 3\,M_\odot$ throughout this paper) is assumed to form a protoplanetary disk with a radius of 100 au, to facilitate a direct comparison with our previous work (M. Patel et al. 2023; R. J. Parker et al. 2023)—though we note that other prescriptions for setting the disk radius as a function of stellar mass are used in the literature (e.g., G. A. L. Coleman & T. J. Haworth 2022). Our disks have a fixed mass dependent on the stellar mass following the formula

$$M_{\rm disk} = 0.1\,M_\star, \quad (2)$$

with a resultant dust mass of $M_{\rm dust} = 0.01\,M_{\rm disk}$. After the dust mass is calculated we calculate the quantity of the SLR's stable-isotope counterparts. We assume a stable aluminum mass fraction of

$$M_{^{27}\rm Al} = 0.0085\,M_{\rm dust}, \quad (3)$$

and a stable iron mass fraction of

$$M_{^{56}\rm Fe} = 0.1828\,M_{\rm dust}, \quad (4)$$

as described in K. Lodders (2003). There is no initial quantity of the SLR isotopes ^{26}Al and ^{60}Fe; all enrichment is assumed to occur post–star formation. Disk truncation through stellar winds and ionizing-radiation flux are not simulated, but could be included in successive versions of this model. The lifetime of each protoplanetary disk is precalculated and derived from an exponential probability density function of the form

$$p(x,\,\beta) = \frac{1}{\beta}e^{-x/\beta}, \quad (5)$$

where p is the probability density, and β is the mean lifetime of a protoplanetary disk. We adopt a value of $\beta = 2$ Myr for the mean disk lifetime, consistent with the findings in A. J. W. Richert et al. (2018). An example of the disk population over time can be seen in Figure 1. Stars with masses above $3\,M_\odot$ are not assigned disks, as they are markedly less likely to form planetary systems containing rocky bodies (O. Berné et al. 2024; M. P. Ronco et al. 2024). Final enrichment is calculated at the point where the individual disk has "progressed" from a disk to a protoplanetary system. Beyond this point, the system is no longer capable of further SLR pollution, and the final enrichment value is stored. A more advanced model could reduce the efficiency of the disk in absorbing SLRs as planetesimals begin to form, before culminating in a finished protoplanetary system, though for our work this two-phase method should suffice.

2.3. SLR Enrichment

For this paper we only simulate the effect of wind and SNae-based enrichment of the protoplanetary disk. SLR enrichment from other mechanisms such as sequential star formation, spallation or molecular cloud pre-enrichment are not considered. Estimates for wind and SNae yields of SLRs from massive stars were derived from simulations performed in M. Limongi & A. Chieffi (2018). For this paper we use their recommended ("R") model with a star rotational velocity of $300\,{\rm km\,s^{-1}}$. There is a small difference in ^{26}Al yield in the $150\,{\rm km\,s^{-1}}$ model and the $300\,{\rm km\,s^{-1}}$ model between $13\,M_\odot$ and $20\,M_\odot$, though for the $20\,M_\odot$ case there is a higher yield in the $150\,{\rm km\,s^{-1}}$ model. The $0\,{\rm km\,s^{-1}}$ model was not considered as this was unrealistic (all massive stars are thought to rotate, though the exact velocity is under debate; S. E. de Mink et al. 2013), and significantly suppressed ^{26}Al yields compared to the

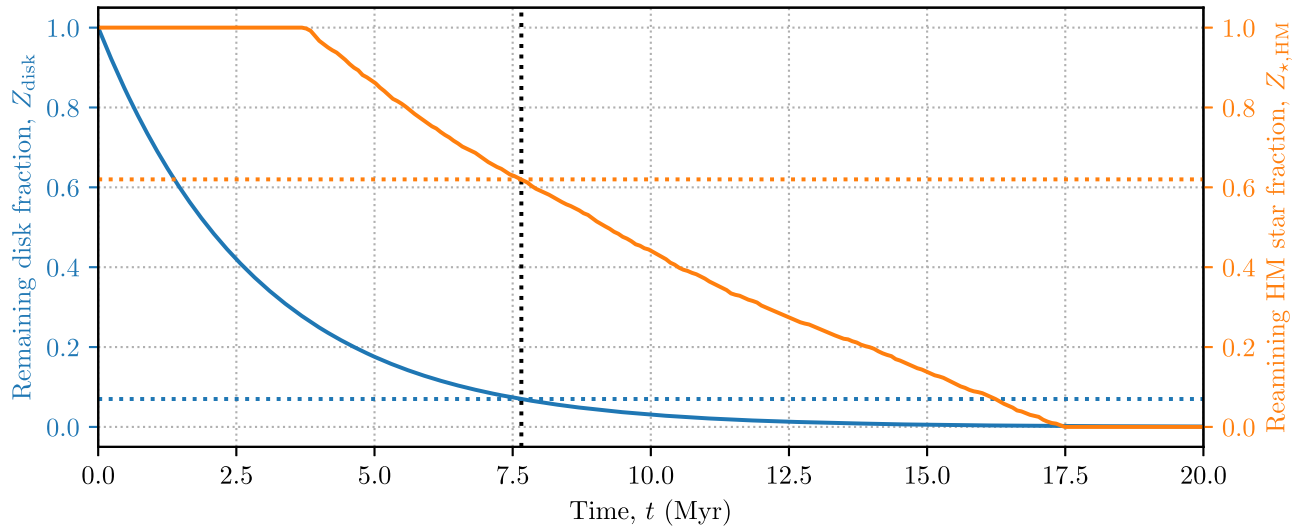

Figure 1. A comparison between the fraction of remaining disks and the fraction of high-mass stars that have not reached the end of their lives. Due to the relatively short disk lifetime most of the stellar disks have progressed to the planetesimal-formation phase before most SNae have occurred. The dotted vertical line indicates when the first stars with an initial mass under 25 $M_\odot$ undergo SNae, contributing to SLR enrichment according to M. Limongi & A. Chieffi (2018).

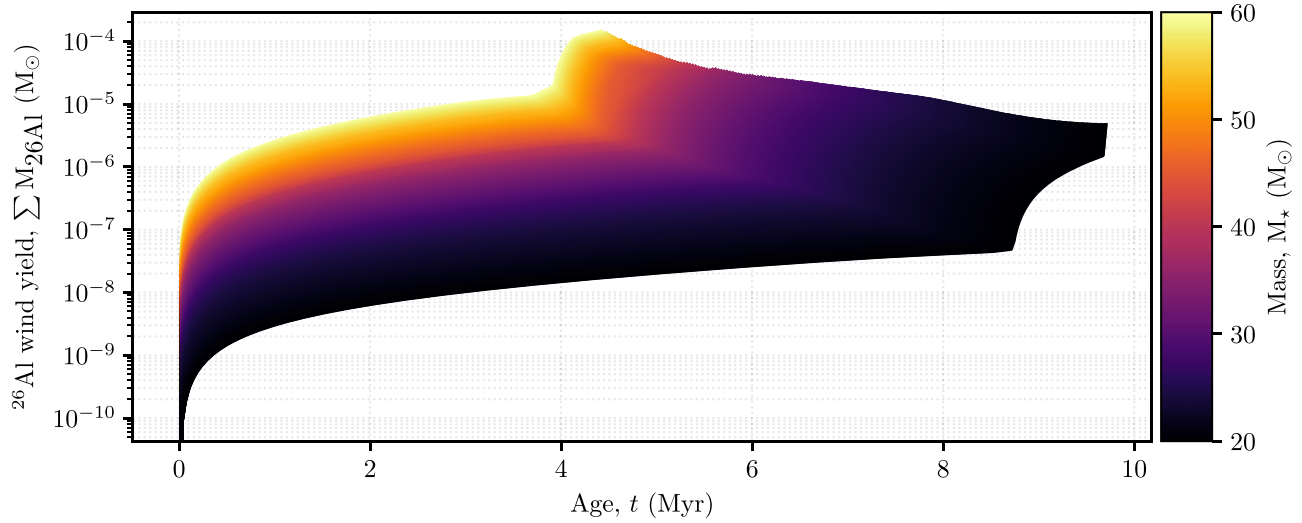

Figure 2. A comparison of cumulative yield of ^{26}Al in stellar winds over 10 Myr from stars with a mass range of 20–60 $M_\odot$. The majority of the mass loss occurs near the end of each star's life, as the star exits the main sequences and begins its Wolf–Rayet phase.

other two options. The results in M. Limongi & A. Chieffi (2018) provide a final total yield; using this value we calculate the fraction of SLR emitted relative to the total wind mass-loss rate using `SeBa` to calculate the total mass-loss rate before the simulation begins. The estimated fraction is calculated through an Akima spline interpolation of the data provided in the paper, which provides a more accurate fit compared to a cubic spline. This fraction can then be used in conjunction with the simulation mass-loss rate from `SeBa` to approximate the SLR emission rate from massive stars. While directly calculating the SLR loss rate through their model would yield improved results—as our estimation does not factor in composition changes in the wind through stellar interior processes such as dredge-up—these issues are offset by the fact that the majority of the mass loss of early-type stars occurs after they leave the main sequence in a comparatively short period of time before (see Figure 2). This method also works for SLRs beyond ^{26}Al and ^{60}Fe, such as ^{36}Cl, ^{41}Ca, and ^{53}Mn, with a minimal increase in computational time per SLR; however, these were not considered for this paper. Future versions of this code will be able to analyze other SLRs, as the routines governing enrichment and decay were designed with flexibility in mind.

In the case of SNae, the total explosive yield of SLRs is provided by M. Limongi & A. Chieffi (2018). It is important to note that the M. Limongi & A. Chieffi (2018) model assumes that stars above 25 $M_\odot$ collapse directly into a black hole, producing no SN explosion and thus resulting in no further enrichment. The debate on this facet of stellar evolution is still ongoing; the mass border wherein SNae occur is still somewhat ill-defined, though contemporary research suggests that SNae become increasingly rare above 20 $M_\odot$ (K. Ebinger et al. 2020; T. Ertl et al. 2020). We determined that for this paper we would not consider these higher-mass SNae—in particular due to the rarity of higher-mass precursor stars—though investigating the effect of higher-mass SNae on star-forming-region enrichment could be a future avenue of research.

2.3.1. Disk Enrichment from Stellar Winds

In order to determine the quantity of material swept up by the protoplanetary disk, we must calculate the geometric cross section of the disk when interacting with the wind. To perform this calculation we approximate the outflow as a spherical wind-blown bubble with a constant density. From this we can calculate the sweep-up area, $\eta_{\rm sweep}$, equivalent to

$$\eta_{\rm sweep} = \frac{3}{4}\frac{r_{\rm disk}^2 \Delta r_\star}{r_{\rm bub}^3}, \tag{6}$$

where $r_{\rm disk}$ is the disk radius, $\Delta r_\star$ is the distance traveled by the approaching star during a time step, and $r_{\rm bub}$ is the bubble radius. Two bubble radii are considered: a small bubble, with a radius of 0.1 pc, and a variable bubble size with a radius equivalent to the current virial radius of the region. These are representative of a small, local wind (the "local" model), and a diffuse, dispersed stellar wind throughout the region (the "global" model) respectively. The total effective cross section from wind absorption, $\eta_{\rm wind}$, is given by the equation

$$\eta_{\rm wind} = \eta_{\rm con}\eta_{\rm inj}\eta_{\rm sweep}, \tag{7}$$

where $\eta_{\rm con}$ is the dust condensation efficiency and $\eta_{\rm inj}$ is the disk injection efficiency. For this paper, $\eta_{\rm con} = 0.5$ (T. Lichtenberg et al. 2016) and $\eta_{\rm inj} = 0.7$ (N. Ouellette et al. 2009). These parameters can vary based on the properties of the massive star and the disk, though these represent somewhat conservative values for both (M. Matsuura et al. 2011), with the bubble radius being the most influential free parameter. Finally, we can calculate the mass sweep-up rate, $\dot{\Gamma}_{\rm wind,SLR}$, of ^{26}Al and ^{60}Fe from the wind-blown bubble using the formula

$$\dot{\Gamma}_{\rm wind,SLR} = \eta_{\rm wind}\dot{M}_{\rm SLR}, \tag{8}$$

where $\dot{M}_{\rm SLR}$ is SLR ejection rate of the massive star.

The "global" and "local" models are run concurrently, as they have no influence on the N-body trajectories nor stellar evolution of the stars within the star-forming region. Additionally, radioactive decay is modeled as the simulation run time and is significantly longer than the half-life of either SLR. Decay is calculated by determining the fraction of remaining SLRs between each time step, based on the ^{26}Al and ^{60}Fe half-lives of 0.7 Myr and 2.6 Myr, respectively.

2.3.2. Disk Enrichment from Supernovae

SNae enrichment is calculated directly from the SN yield of the star. All stars within the star-forming region are instantaneously injected with SLRs. While the outflow material from the SN would not be traveling instantaneously, the crossing time of the outflow is on the order of 100 yr, significantly smaller than the smallest simulation time step of 2×10^4 yr, and as such this is a reasonable abstraction. The amount of material from the SN deposited onto a protoplanetary disk is dependent on the cross-sectional area of the disk relative to the SN, such that the geometric efficiency, $\eta_{\rm geom}$, is

$$\eta_{\rm geom} = \frac{\pi r_{\rm disk}^2 \cos\theta}{4\pi d^2}, \tag{9}$$

where d is the distance from the approaching star and θ is the disk inclination relative to the massive star. We assume a constant disk inclination of 60°, such that $\cos\theta = 0.5$. The total SN SLR absorption efficiency, $\eta_{\rm SNae}$, is given by the equation

$$\eta_{\rm SNe} = \eta_{\rm con}\eta_{\rm inj}\eta_{\rm geom}, \tag{10}$$

with the same values detailed in Section 2.3.1. From this we calculate the SNae injection mass, $\Gamma_{\rm SNae,SLR}$, of both SLRs with the following equation:

$$\Gamma_{\rm SNe,SLR} = \eta_{\rm SNe}M_{\rm SNe,SLR}, \tag{11}$$

where $M_{\rm SNae,SLR}$ is the SLR yield from the SN.

2.4. Simulation Postprocessing

Enrichment through the "global" model and the SNae-resultant enrichment are calculated using a postprocessing method that calculates the enrichment rates at each simulation checkpoint, while enrichment through the "local" model is calculated at the end of each N-body time step. Both methods are very fast, with postprocessing through the global model taking a few seconds per simulation on a reasonably powerful desktop PC, while the local model takes 5%–10% of the total computational time per simulation step on the same computer. The main source of compute time is the calculation of distances between high-mass and low-mass stars. Adding more SLRs for consideration would not impact performance significantly as calculating the enrichment rate is comparatively simple. The contributions through each model are collated as part of a final postprocessing step, which is performed before plots were made.

3. Results

We performed repeated simulations with varying star number densities by modifying the star-forming-region radius and number of stars within the star-forming region. The number of stars, $N_\star$ is varied between 100, 1000, and 10^4 stars, in order to observe the effect of star number density (ρ_c) and the compound effect of multiple massive stars and SNae. The star-forming-region radius is varied between 0.3, 1.0, and 3.0 pc, to provide representative examples of extremely compact, compact, and dispersed star-forming regions. This correlates to extremely dense and relatively dispersed star-forming regions, and is done in order to differentiate between effects due to region density and massive star count. Each set of parameters is repeated 32 times, to reduce the statistical impact of systems enriched through improbable means such as multiple SNae passes (Table 1).

An important factor governing the enrichment of disks within these simulations is that the rate of disk progression is significantly faster than the average rate of SNae occurring for any given simulation. While massive stellar winds make up the bulk of ^{26}Al enrichment, ^{60}Fe enrichment through winds is many orders of magnitude slower, as enrichment relies more heavily on SNae; therefore, ^{60}Fe enrichment is curtailed. Furthermore, we make the same assumption as M. Limongi & A. Chieffi (2018) that only stars with an initial mass below 25 $M_\odot$ produce SNae, with stars higher than this initial mass instead directly collapsing into black holes. As such, enrichment from SNae does not occur until ∼7 Myr after the start of the simulation, at a point where only 7% of disks remain, as seen in Figure 1.

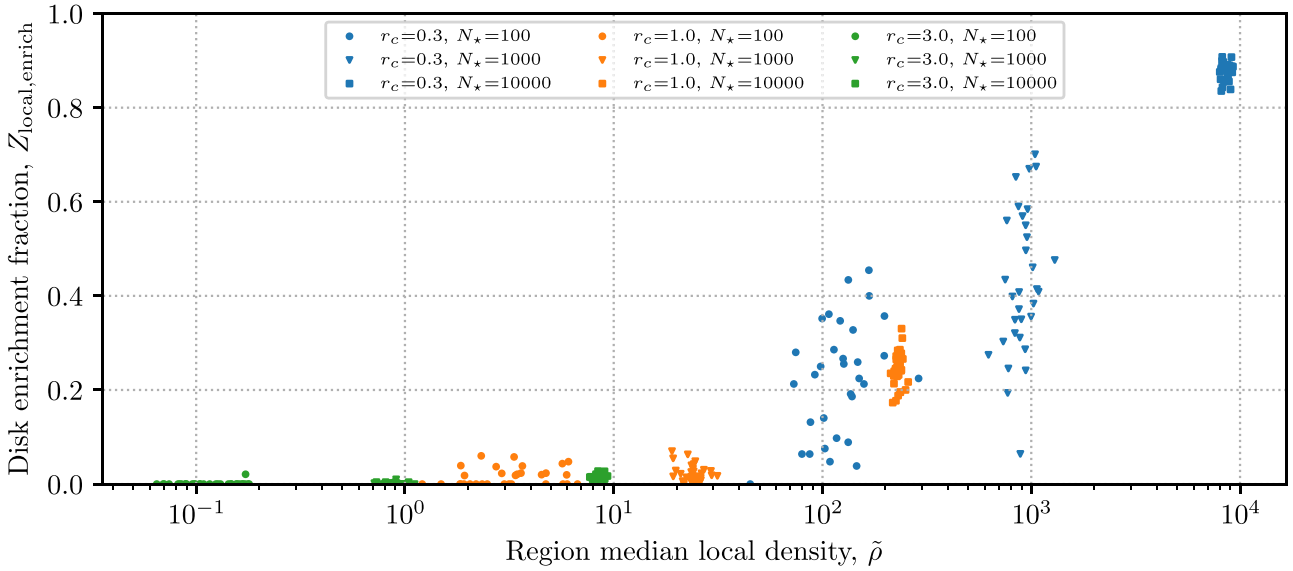

Figure 3. A plot of all simulations showing the fraction of all stellar disks that underwent any amount of enrichment from the local wind model vs. initial median local density. We observe a clear dependence on region density, which is more important than the number of stars in the region, despite simulations with a higher number of stars inherently having more massive stars.

Table 1

A Table Showing the Simulation Parameters as Well as a Number of Key Parameters, the Mean High-mass Star Count in the Simulation $N_{\star,\rm HM}$, the Mean Number of SNae by the End of the Simulation $N_{\rm SNae}$, the Fraction of Disks Enriched by the Local Model, $Z_{\rm local,enrich}$, and the Fraction of Disks Undergoing ^{26}Al Enrichment Approaching Solar System Estimates (0.1× Solar Value), $Z_{\rm 26Al,0.1SS}$

Set Name	R_c	$N_\star$	$N_{\star,\rm HM}$	$N_{\rm SNae}$	$Z_{\rm local,enrich}$	$Z_{\rm 26Al,0.1SS}$
pt-0.3-100-fr	0.3	100	1.125 ± 0.074	0.781 ± 0.098	0.223 ± 0.022	0.063 ± 0.021
pt-0.3-1000-fr	0.3	1000	2.719 ± 0.278	1.500 ± 0.201	0.426 ± 0.027	0.046 ± 0.012
pt-0.3-10000-fr	0.3	10000	20.031 ± 0.667	13.531 ± 0.582	0.877 ± 0.003	0.502 ± 0.026
pt-1.0-100-fr	1.0	100	1.062 ± 0.043	0.844 ± 0.079	0.015 ± 0.003	0.003 ± 0.002
pt-1.0-1000-fr	1.0	1000	2.188 ± 0.213	1.375 ± 0.140	0.023 ± 0.003	0.003 ± 0.001
pt-1.0-10000-fr	1.0	10000	19.344 ± 0.823	12.531 ± 0.592	0.244 ± 0.007	0.024 ± 0.003
pt-3.0-100-fr	3.0	100	1.094 ± 0.052	0.844 ± 0.091	0.001 ± 0.001	0.001 ± 0.001
pt-3.0-1000-fr	3.0	1000	2.594 ± 0.245	1.906 ± 0.203	0.001 ± 0.000	0.000 ± 0.000
pt-3.0-10000-fr	3.0	10000	21.000 ± 0.779	14.438 ± 0.654	0.015 ± 0.001	0.001 ± 0.000

Note. It is important to note that for 100-star simulations there is a significantly higher fraction of massive stars, due to the requirement of a high-mass star in each simulation.

3.1. Population Statistics

Table 1 contains detailed statistics of each simulation set, in particular the number of high-mass stars ($N_{\star,\rm HM}$), simulation SNae count ($N_{\rm SNae}$), fraction of disks undergoing enrichment ($Z_{\rm local,enrich}$), and the fraction of disks that underwent enough enrichment for significant degassing to occur (defined as 0.1 × solar system enrichment, $Z_{\rm 26Al,0.1SS}$). Enrichment calculations are based on the local model.

To calculate the density of a star-forming region in these simulations we use the initial median local density (R. J. Parker 2014; R. J. Parker et al. 2021). This value is calculated by determining the median value of the stellar density of a sphere containing the 10 nearest stars to each star in the star-forming region at the start of the simulation. Figure 3 compares the fraction of all disks that underwent any form of enrichment under the local model versus the median local density. This nonzero enrichment fraction is used to show how likely close passes to massive stars are for disks. We find that the amount of disks undergoing enrichment for any given simulation is highly dependent on the initial median local density of the star-forming region. This suggests that a compact, low-population star-forming region with a single massive star is potentially ideal for SLR enrichment. Such region masses would be significantly more likely to occur in nature than higher-mass star-forming regions, and the number of low-mass regions containing a single massive star is similar to the number of higher-mass regions that always contain massive stars (R. B. Nicholson & R. J. Parker 2017). Furthermore, the lower massive star count would result in less disk disruption due to ionizing-photon flux and SNae shocks (R. B. Nicholson et al. 2019; M. Patel et al. 2023). Even in the case of extremely large numbers of stars, region radius and density appear to be more influential than star counts in keeping massive stellar winds distant from disks. It should be noted that the 100-star systems have a higher fraction of massive stars to low-mass stars, due to the minimum simulation requirement of one massive star. The percentage of massive stars in simulations with 100 stars is ∼1.1% compared to ∼0.25% of the more populous simulations. This can potentially overestimate the amount of enrichment in a particular system;

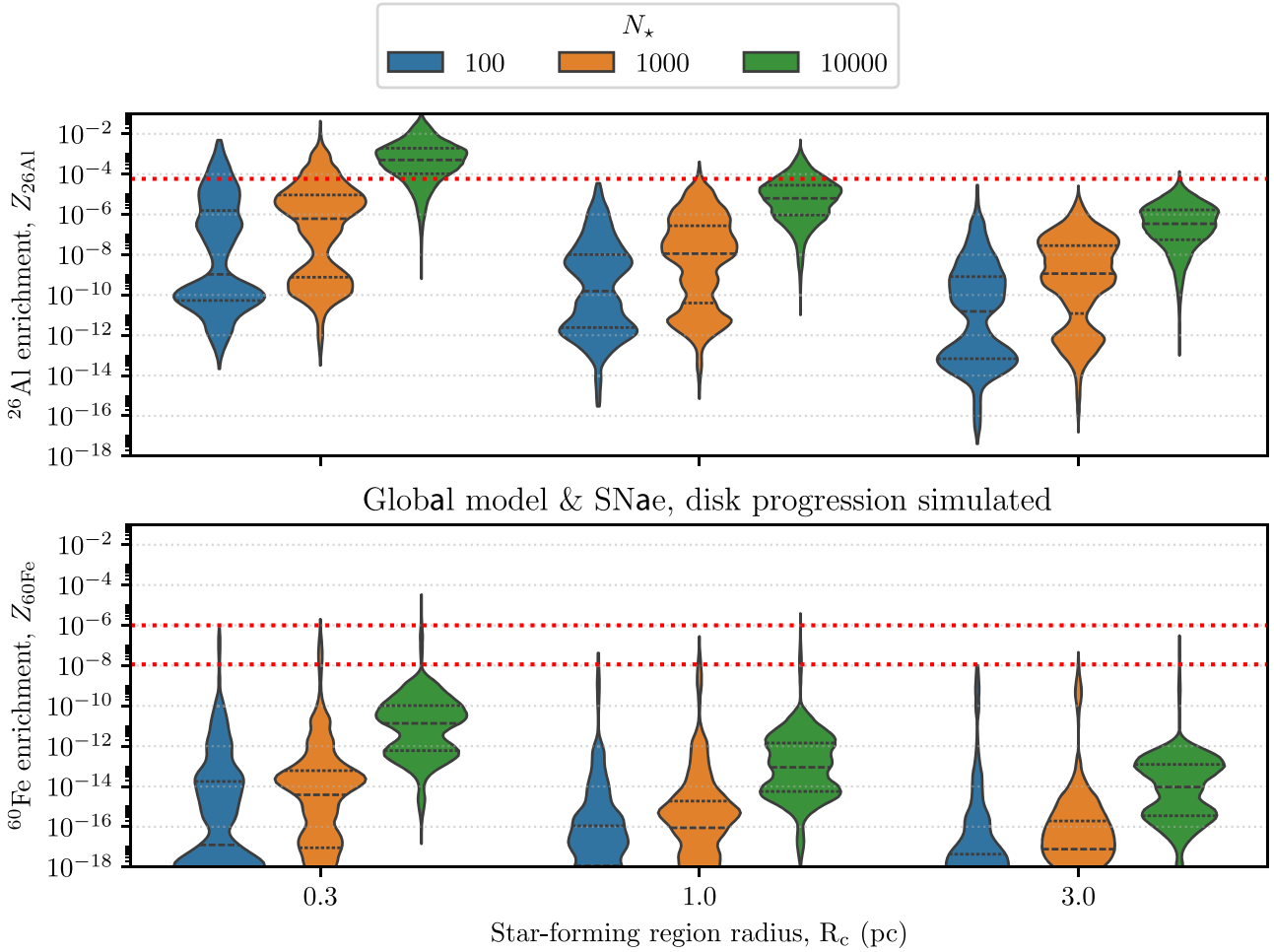

Figure 4. A series of violin plots detailing ^{26}Al and ^{60}Fe enrichment. Solar system enrichment is shown as a red dashed line; a value of $Z_{26Al,SS} \approx 5 \times 10^{-5}$ is used for the ^{26}Al graphs (K. Thrane et al. 2006), while a low value of $Z_{60Fe,SS} = 10^{-8}$ and a high value of $Z_{60Fe,SS} = 10^{-6}$ are used for ^{60}Fe plots (H. Tang & N. Dauphas 2012; R. K. Mishra et al. 2016). The enrichment values are calculated at the point where the disk has "progressed" or at the end of the simulation, whichever is shortest. While there is a higher amount of ^{26}Al enrichment, the primarily SNae-driven ^{60}Fe enrichment is suppressed as most disks may not undergo SNae interaction.

however, simulating systems without an SLR source would have been redundant.

3.2. Comparison Between Models

Figure 4 shows enrichment values calculated at the end of the disk's lifetime. Wind enrichment is influential, as can be seen in the ^{26}Al results, as ^{60}Fe enrichment is extremely minimal (though not zero) through stellar winds. We see that for low-radius star-forming regions there are a significant number of stars with ^{26}Al enrichment greater than the solar system estimate; however, for regions with a higher radius we see that this drops off rapidly, with only the simulation set where $r_c = 1$ pc and $N_\star = 10^4$ exceeding the solar system average.

In the case of ^{60}Fe enrichment there is an even greater discrepancy between the two models, as the ^{60}Fe yield from SNae is multiple orders of magnitude greater than the total wind yield from a massive star; ^{60}Fe enrichment relies almost entirely on SNae. As disk population is reduced when SNae begin to occur (see Figure 1) we find that there is a vanishingly small population of stars that have solar-system-like levels of ^{60}Fe enrichment. The longer half-life of ^{60}Fe does not contribute much to increasing the final enrichment of disks, whereas for ^{26}Al it was extremely significant. As we discussed in our previous paper (J. W. Eatson et al. 2024), ^{60}Fe enrichment is only important for the evolution and desiccation of planetesimals in the case of extremely high levels of enrichment ($Z_{60Fe} \gtrapprox 10^{-2}$ or $10^4 \times Z_{60Fe,SS}$). Our results in Figure 4 show that these levels of enrichment would be almost impossible, and nothing even close was observed in our suite of simulations.

We can infer from these results that disk lifetimes are highly influential in the calculation of SLR enrichment. SLRs that make up a significant fraction of the stellar wind, such as ^{26}Al, are continuously distributed over the lifespan of the massive stars within the star-forming region. However, the shorter half-life of ^{26}Al results in significantly skewed results if the measurement of final ^{26}Al enrichment occurs at the end of the simulation. Furthermore, disks that survive long enough that a local star enters the Wolf–Rayet phase and goes SN will see a significantly increased ^{26}Al enrichment, as well as some ^{60}Fe enrichment.

Figure 5 shows the results for simulations where the "local" model is used instead; we observe that a greater number of disks become highly ^{26}Al enriched, and in some cases can be enriched more than 2 orders of magnitude higher than the solar system baseline. However, it should be noted that with the "local" model a disk system can have zero enrichment, which would not be represented in the violin plot. Enrichment

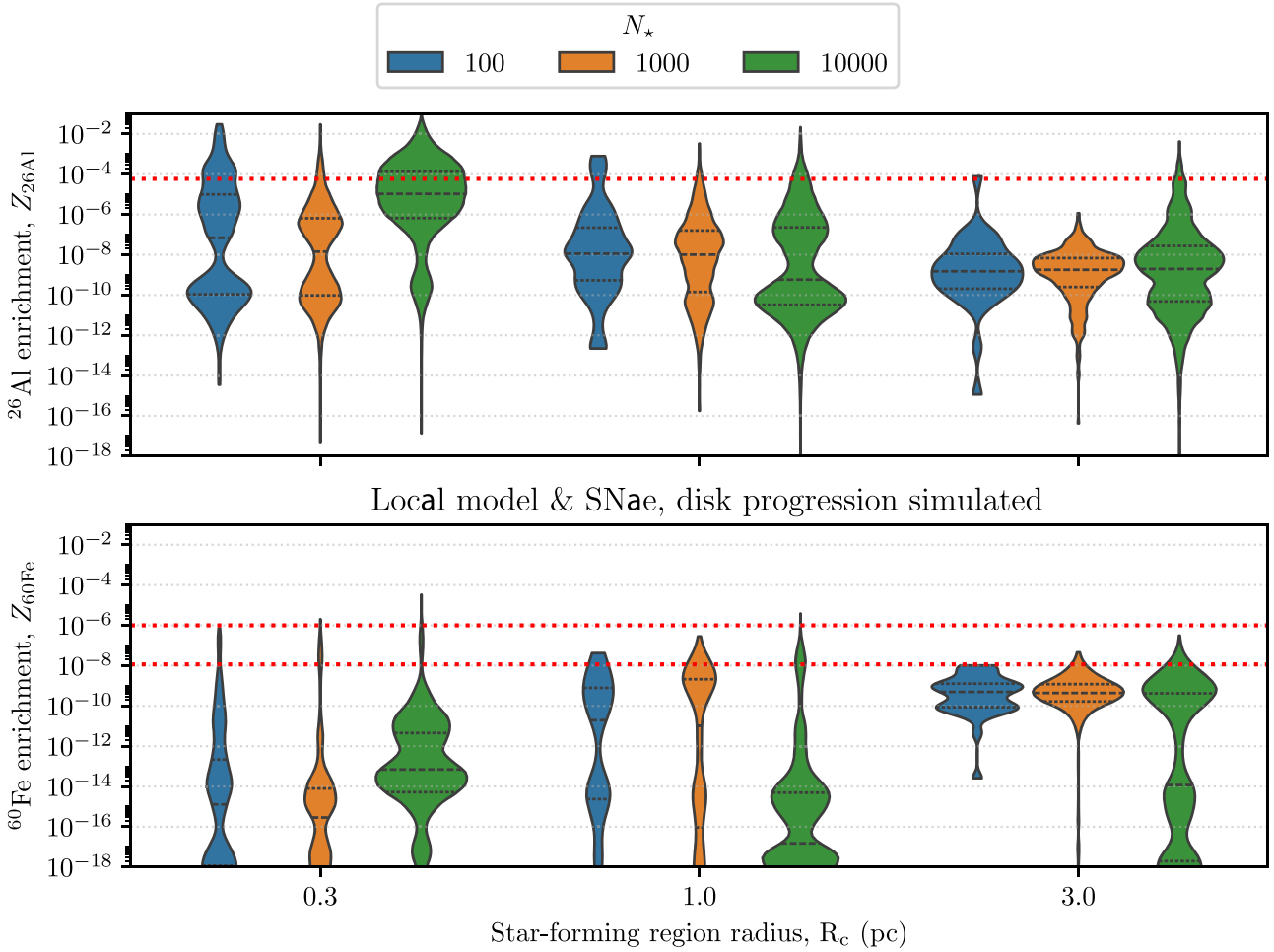

Figure 5. A series of violin plots showing ^{26}Al and ^{60}Fe enrichment. Enrichment is calculated through the local model while disk progression is simulated in a similar manner to Figure 4. Solar system enrichment is shown as a red dashed line; a value of $Z_{26Al,SS} \approx 5 \times 10^{-5}$ is used for the ^{26}Al graphs (K. Thrane et al. 2006), while a low value of $Z_{60Fe,SS} = 10^{-8}$ and a high value of $Z_{60Fe,SS} = 10^{-6}$ are used for ^{60}Fe plots (H. Tang & N. Dauphas 2012; R. K. Mishra et al. 2016). Compared to the global model SLR enrichment is significantly elevated; however, many simulations undergo no enrichment whatsoever with this model (see Table 1).

fractions of disks for each simulation set are shown in Table 1. This enrichment fraction is shown in more detail in Figure 6, where we can clearly see a small fraction of disks in compact star-forming regions being enriched to above-solar-system amounts, even in the case of regions with a low overall population of stars. Above-solar-system enrichment can occur in star-forming regions with a higher initial radius, though this is significantly less likely, and is similarly independent of the total number of stars in the region. The total number of systems undergoing ^{60}Fe enrichment is similarly changed, as the SLR flux onto a disk is significantly increased in the local model when a disk is proximal to a massive star. However, this effect does not drastically increase the number of systems with solar-system-like levels of ^{60}Fe, which is still dominated by SNae rather than stellar winds, and as such the impact of accounting for disk lifetimes has a more marked effect on enrichment than the wind model.

From previous work in T. Lichtenberg et al. (2019) and J. W. Eatson et al. (2024) it is found that ^{26}Al is highly important in the process of planetesimal desiccation, with enrichment levels greater than $0.1 \times Z_{26Al,SS}$ causing a reduction in final water retention fraction of larger early planetesimals. Table 1 shows that only a small fraction of disks gain this level of enrichment, requiring compact, dense star-forming regions. The main outlier is the simulation set of regions with 10^4 stars and radii of 0.3 pc; these superdense star-forming regions frequently produce highly enriched disks, though occurrence of such massive star-forming regions is rare, and also the large number of SNae that occur would result in significant disk disruption (R. B. Nicholson & R. J. Parker 2017). It is also important to note that at a radius of 3 pc sufficient enrichment becomes improbable, happening to <0.1% of disks, even in the case of extremely large star counts and SNae counts, as these values are inclusive of SNae deposition. ^{60}Fe enrichment is markedly less influential to planetesimal evolution, due to the radioisotope's lower decay rate, decay energy, and disk mass fraction. In our previous paper we found that extreme levels of ^{60}Fe enrichment ($>10^3 \times Z_{60Fe,SS}$) are required to produce the level of heating that results in desiccation (J. W. Eatson et al. 2024). We find in this paper that solar system levels of enrichment are unlikely, let alone enrichment to 10^3 times solar system amounts. This further rules out ^{60}Fe as an influential SLR for planetesimal heating, and the lack of ^{60}Fe enrichment to solar system amounts in our simulations suggests the presence of alternative mechanisms of ^{60}Fe enrichment beyond SNae—such as AGB stars (R. J. Parker & C. Schoettler 2023). Finally, comparing this result to previous work such as R. J. Parker et al. (2023) we find that ^{26}Al contribution from stellar winds is very significant, and that stellar density is very important. As we vary both the

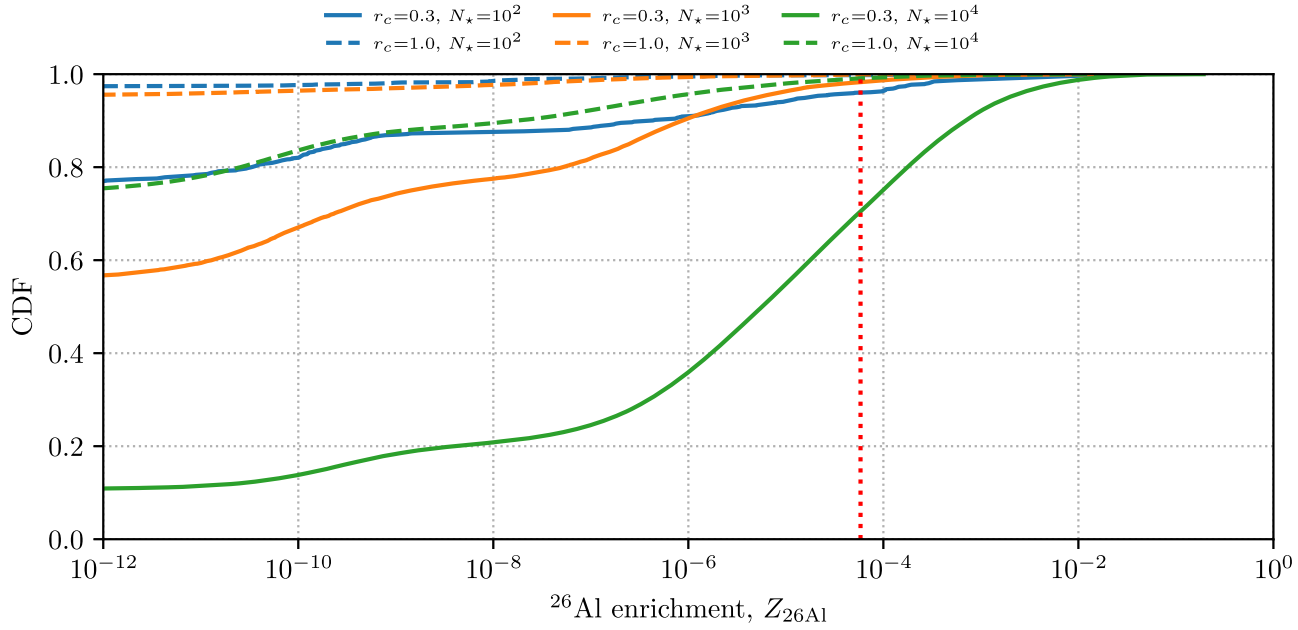

Figure 6. A cumulative distribution function of final ^{26}Al enrichment fraction (Z_{Al}) for all disks grouped by subset with disk progression simulated. A significant population of disks have a higher enrichment fraction than the solar system upon entering the planetesimal-formation phase in the cases of systems with extremely large numbers of stars.

star-forming region and total population we find that more compact star-forming regions produce greater levels of both ^{26}Al and ^{60}Fe enrichment, and radius is more influential on enrichment than population, especially in the case of the local wind bubble model.

4. Discussion

Comparing the disks generated in this simulation with the solar protoplanetary disk, we find that initial solar system abundances for both ^{26}Al and ^{60}Fe do occur, but are typically less common. This suggests that the solar system is on the upper end of SLR enrichment, except in the case of very dense, populous ($N_\star > 10{,}000$) star-forming regions. These results also suggest that the probability of ocean worlds is relatively high, as radioisotopic heating would be insufficient to cause significant devolatilization in planetesimals, resulting in a significantly higher water budget for a "typical" nascent protoplanet (T. Lichtenberg et al. 2019; J. W. Eatson et al. 2024). An expanded, more quantitative study would be necessary to estimate the population of ocean worlds in more detail. In recent years the physical cause of the density dichotomy between super-Earths and sub-Neptune exoplanets has come under closer scrutiny by formation models that involve water enrichment during the disk phase (e.g., R. Burn et al. 2024; J. Venturini et al. 2024) instead of solely relying on postdisk atmospheric escape. Hence, a population synthesis or statistical approach involving ^{26}Al desiccation with more modern formation models (e.g., T. Kimura & M. Ikoma 2022) appears a natural extension for future work to interpret the growing data from the low-mass exoplanet census (T. Lichtenberg & Y. Miguel 2024).

Star count does not particularly increase the maximum ^{26}Al enrichment, though can result in more disks being significantly enriched; instead we find that star-forming-region mass density significantly affects the final disk enrichment. This is the case even with the "global" wind model, as the rate of SLR deposition is significantly curtailed as the bubble radius is larger. In the more common case of compact, low-mass star-forming regions, we find that around 5% of disks have undergone levels of enrichment on the order of our solar system, enough for ^{26}Al decay heating to have a pronounced effect on planetesimal evolution, particularly affecting retained water fraction. While massive stellar winds and SNae are a prominent source of SLRs, the adverse affects of UV photoevaporation and SNae shocks can disrupt disks before planetesimals form (M. Patel et al. 2023), making (typically low-mass) star-forming regions with fewer massive stars more conducive to planet formation. As such, the combination of high levels of SLRs in lower-population star-forming regions would result in more water-poor rocky planets. Incorporating disk progression and measuring the final enrichment from the moment the disk has decayed is a more accurate method of determining enrichment, and in the case of ^{26}Al with its significantly shorter half-life, this can significantly impact results compared to an observation at an arbitrary time or the end of the simulation. In the case of ^{60}Fe, however, we find that SN-based enrichment is severely inhibited by the disk lifetime typically being significantly shorter than the lifetime of high-mass stars. We find that by the time SNae begin to occur only a quarter of protoplanetary disks remain (Figure 1), this is also seen in our results where disk "decay" skews the ^{60}Fe yields down more than any contributing factor. This is further inhibited when factoring in high-mass stars failing to undergo SNae. These results are corroborated by the findings of J. P. Williams & E. Gaidos (2007) and M. Gounelle & A. Meibom (2008), whose results suggest a similar unlikelihood of solar-system-level enrichment, and only in large clusters with very high-mass stars. The "R" model described in M. Limongi & A. Chieffi (2018) assumes that direct black-hole collapse occurs when a star with an initial mass greater than 25 $M_\odot$ dies, resulting in zero SLR yield. At the point where these contributing SNae begin to occur, less than 10% of all disks remain, resulting in further inhibited ^{60}Fe enrichment. While our model does not take into account mixed-age stellar

populations, we do not believe that this would significantly impact our results, and would be offset by other unsimulated interactions, such as evaporation of disks from UV flux from massive stars and SNae shocks (M. Patel et al. 2023). Furthermore, the "low" ($Z_{^{60}Fe/^{56}Fe,SS} \approx 10^{-8}$) ^{60}Fe solar system estimate from H. Tang & N. Dauphas (2012) can be explained through processes such as residual galactic chemical evolution; this mechanism does not explain the higher enrichment levels determined by other studies, such as R. K. Mishra et al. (2016) and D. L. Cook et al. (2021). It appears unlikely that these higher estimates can be explained purely through SNae. Alternative ^{60}Fe injection mechanisms such as interloping AGB stars could prove a suitable explanation for this discrepancy (J. M. Trigo-Rodríguez et al. 2009; A. I. Karakas & M. Lugaro 2016; R. J. Parker & C. Schoettler 2023).

5. Conclusion

In this paper we performed a series of simulations to determine typical enrichment rates of star-forming regions for specific densities and stellar populations. Results differ from previous work (T. Lichtenberg et al. 2016; R. J. Parker et al. 2023), as while we observe a similar amount of ^{26}Al enrichment, the local wind model produces a higher number of disks undergoing ^{26}Al enrichment significant enough to influence planetary evolution. Much of the changes in enrichment compared to previous work are due to the length of time required for SNae to occur, which is much longer than the average time a disk needs to progress. Stratification of enrichment from varying simulation parameters is very clear, with enrichment increasing with star-forming-region mass density. We also find that enrichment method and disk model are particularly influential on the final SLR enrichment amount. ^{26}Al enrichment is primarily through wind deposition—as this is relatively consistent for either model assuming the system is sufficiently populous or dense—when compared to SNae deposition. ^{60}Fe enrichment, however, is almost entirely dependent on SNae deposition, and as such enrichment to solar system levels is unlikely, and enrichment to levels where ^{60}Fe is the dominant heating source of planetesimals is almost nonexistent.

In the immediate future, including additional SLR sources such as from "interloping" AGB stars would provide an interesting comparison. As ^{60}Fe is formed in the core of more massive AGB stars and can be efficiently dredged up and deposited via the stellar wind—this could result in another avenue of ^{60}Fe enrichment in lieu of the relatively ineffective massive-stellar-wind mechanism (R. J. Parker & C. Schoettler 2023).

Acknowledgments

J.W.E. and R.J.P. acknowledge support from the Royal Society in the form of a Dorothy Hodgkin fellowship, and associated enhancement awards. T.L. acknowledges support by the Branco Weiss Foundation, the Alfred P. Sloan Foundation (AEThER project, G202114194), and NASA's Nexus for Exoplanet System Science research coordination network (Alien Earths project, 80NSSC21K0593).

ORCID iDs

Joseph W. Eatson https://orcid.org/0000-0002-5160-8871
Richard J. Parker https://orcid.org/0000-0002-1474-7848
Tim Lichtenberg https://orcid.org/0000-0002-3286-7683

References

Alves, F. O., Cleeves, L. I., Girart, J. M., et al. 2020, ApJL, 904, L6
Barnes, J., & Hut, P. 1986, Natur, 324, 446
Berné, O., Habart, E., Peeters, E., et al. 2024, Sci, 383, 988
Brinkman, H. E., den Hartogh, J. W., Doherty, C. L., Pignatari, M., & Lugaro, M. 2021, ApJ, 923, 47
Brinkman, H. E., Doherty, C., Pignatari, M., Pols, O., & Lugaro, M. 2023, ApJ, 951, 110
Burn, R., Mordasini, C., Mishra, L., et al. 2024, NatAs, 8, 463
Cartwright, A., & Whitworth, A. P. 2004, MNRAS, 348, 589
Coleman, G. A. L., & Haworth, T. J. 2022, MNRAS, 514, 2315
Cook, D. L., Meyer, B. S., & Schönbächler, M. 2021, ApJ, 917, 59
Daffern-Powell, E. C., & Parker, R. J. 2020, MNRAS, 493, 4925
Dale, J. E., Ercolano, B., & Bonnell, I. A. 2012, MNRAS, 424, 377
Dale, J. E., Ercolano, B., & Bonnell, I. A. 2013, MNRAS, 430, 234
de Mink, S. E., Langer, N., Izzard, R. G., Sana, H., & de Koter, A. 2013, ApJ, 764, 166
Dib, S., Schmeja, S., & Parker, R. J. 2018, MNRAS, 473, 849
Dodds, K. H., Bryson, J. F. J., Neufeld, J. A., & Harrison, R. J. 2021, JGRE, 126, e2020JE006704
Drazkowska, J., Bitsch, B., Lambrechts, M., et al. 2023, in ASP Conf. Ser. 534, Protostars and Planets VII, ed. S. Inutsuka et al. (San Francisco, CA: ASP), 717
Eatson, J. W., Lichtenberg, T., Parker, R. J., & Gerya, T. V. 2024, MNRAS, 528, 6619
Ebinger, K., Curtis, S., Ghosh, S., et al. 2020, ApJ, 888, 91
Ertl, T., Woosley, S. E., Sukhbold, T., & Janka, H.-T. 2020, ApJ, 890, 51
Gabriel, E., Fagg, G. E., Bosilca, G., et al. 2004, in Proc. 11th European PVM/MPI Users' Group Meeting, ed. D. Kranzlmüller, P. Kacsuk, & J. Dongarra (Berlin: Springer), 97
Gaidos, E., Krot, A. N., Williams, J. P., & Raymond, S. N. 2009, ApJ, 696, 1854
Girichidis, P., Federrath, C., Allison, R., Banerjee, R., & Klessen, R. S. 2012, MNRAS, 420, 3264
Goodwin, S. P., & Whitworth, A. P. 2004, A&A, 413, 929
Gounelle, M., & Meibom, A. 2008, ApJ, 680, 781
Gounelle, M., & Meynet, G. 2012, A&A, 545, A4
Grewal, D. S., Nie, N. X., Zhang, B., Izidoro, A., & Asimow, P. D. 2024, NatAs, 8, 290
Jacobsen, B., Yin, Q.-z., Moynier, F., et al. 2008, E&PSL, 272, 353
Karakas, A. I., & Lugaro, M. 2016, ApJ, 825, 26
Kimura, T., & Ikoma, M. 2022, NatAs, 6, 1296
Kita, N. T., Yin, Q.-Z., MacPherson, G. J., et al. 2013, M&PS, 48, 1383
Krijt, S., Kama, M., McClure, M., et al. 2023, in ASP Conf. Ser. 534, Protostars and Planets VII, ed. S. Inutsuka et al. (San Francisco, CA: ASP), 1031
Lichtenberg, T., & Clement, M. S. 2022, ApJL, 938, L3
Lichtenberg, T., Golabek, G. J., Burn, R., et al. 2019, NatAs, 3, 307
Lichtenberg, T., & Krijt, S. 2021, ApJL, 913, L20
Lichtenberg, T., & Miguel, Y. 2024, TrGeo, 7, 51
Lichtenberg, T., Parker, R. J., & Meyer, M. R. 2016, MNRAS, 462, 3979
Lichtenberg, T., Schaefer, L. K., Nakajima, M., & Fischer, R. A. 2023, in ASP Conf. Ser. 534, Protostars and Planets VII, ed. S. Inutsuka et al. (San Francisco, CA: ASP), 907
Limongi, M., & Chieffi, A. 2018, ApJS, 237, 13
Lodders, K. 2003, ApJ, 591, 1220
Lugaro, M., Ott, U., & Kereszturi, Á. 2018, PrPNP, 102, 1
Manara, C. F., Ansdell, M., Rosotti, G. P., et al. 2023, in ASP Conf. Ser. 534, Protostars and Planets VII, ed. S. Inutsuka et al. (San Francisco, CA: ASP), 539
Maschberger, T. 2013, MNRAS, 429, 1725
Matsuura, M., Dwek, E., Meixner, M., et al. 2011, Sci, 333, 1258
Mishra, R. K., Marhas, K. K., & Sameer 2016, E&PSL, 436, 71
Monteux, J., Golabek, G. J., Rubie, D. C., Tobie, G., & Young, E. D. 2018, SSRv, 214, 39
Newcombe, M. E., Nielsen, S. G., Peterson, L. D., et al. 2023, Natur, 615, 854
Nicholson, R. B., & Parker, R. J. 2017, MNRAS, 464, 4318
Nicholson, R. B., Parker, R. J., Church, R. P., et al. 2019, MNRAS, 485, 4893
Ouellette, N., Desch, S. J., Bizzarro, M., et al. 2009, GeCoA, 73, 4946
Palacios, A., Meynet, G., Vuissoz, C., et al. 2005, A&A, 429, 613
Parker, R. J. 2014, MNRAS, 445, 4037
Parker, R. J. 2020, RSOS, 7, 201271
Parker, R. J., & Goodwin, S. P. 2007, MNRAS, 380, 1271
Parker, R. J., Lichtenberg, T., Patel, M., Polius, C. K. M., & Ridsdill-Smith, M. 2023, MNRAS, 521, 4838
Parker, R. J., & Meyer, M. R. 2012, MNRAS, 427, 637
Parker, R. J., Nicholson, R. B., & Alcock, H. L. 2021, MNRAS, 502, 2665

Parker, R. J., & Schoettler, C. 2023, ApJL, 952, L16
Patel, M., Polius, C. K. M., Ridsdill-Smith, M., Lichtenberg, T., & Parker, R. J. 2023, MNRAS, 525, 2399
Paxton, B., Bildsten, L., Dotter, A., et al. 2011, ApJS, 192, 3
Pelupessy, F. I., van Elteren, A., de Vries, N., et al. 2013, A&A, 557, A84
Portegies Zwart, S., McMillan, S., Harfst, S., et al. 2009, NewA, 14, 369
Portegies Zwart, S. F., McMillan, S. L. W., van Elteren, A., Pelupessy, F. I., & de Vries, N. 2013, CoPhC, 184, 456
Portegies Zwart, S. F., & Verbunt, F. 1996, A&A, 309, 179
Richert, A. J. W., Getman, K. V., Feigelson, E. D., et al. 2018, MNRAS, 477, 5191
Ronco, M. P., Schreiber, M. R., Villaver, E., Guilera, O. M., & Miller Bertolami, M. M. 2024, A&A, 682, A155
Sánchez, N., & Alfaro, E. J. 2009, ApJ, 696, 2086
Segura-Cox, D. M., Schmiedeke, A., Pineda, J. E., et al. 2020, Natur, 586, 228
Tang, H., & Dauphas, N. 2012, E&PSL, 359, 248
Thrane, K., Bizzarro, M., & Baker, J. A. 2006, ApJL, 646, L159
Toonen, S., Nelemans, G., & Portegies Zwart, S. 2012, A&A, 546, A70
Trigo-Rodríguez, J. M., García-Hernández, D. A., Lugaro, M., et al. 2009, M&PS, 44, 627
Venturini, J., Ronco, M. P., Guilera, O. M., et al. 2024, A&A, 686, L9
Wasserburg, G. J., Karakas, A. I., & Lugaro, M. 2017, ApJ, 836, 126
Williams, J. P., & Gaidos, E. 2007, ApJ, 663, L33
Zwart, S. P. 2019, A&A, 622, A69
Zwart, S. P., & McMillan, S. 2018, Astrophysical Recipes: The Art of AMUSE (Bristol: IOP Publishing)